OPTICS

Direct visualization of electromagnetic wave dynamics by laser-free ultrafast electron microscopy

Xuewen Fu[1,2]*, Erdong Wang[3], Yubin Zhao[4], Ao Liu[4], Eric Montgomery[4], Vikrant J. Gokhale[5], Jason J. Gorman[5], Chunguang Jing[4], June W. Lau[6], Yimei Zhu[1]*

Integrating femtosecond lasers with electron microscopies has enabled direct imaging of transient structures and morphologies of materials in real time and space. Here, we report the development of a laser-free ultrafast electron microscopy (UEM) offering the same capability but without requiring femtosecond lasers and intricate instrumental modifications. We create picosecond electron pulses for probing dynamic events by chopping a continuous beam with a radio frequency (RF)–driven pulser with the pulse repetition rate tunable from 100 MHz to 12 GHz. As a first application, we studied gigahertz electromagnetic wave propagation dynamics in an interdigitated comb structure. We reveal, on nanometer space and picosecond time scales, the transient oscillating electromagnetic field around the tines of the combs with time-resolved polarization, amplitude, and local field enhancement. This study demonstrates the feasibility of laser-free UEM in real-space visualization of dynamics for many research fields, especially the electrodynamics in devices associated with information processing technology.

INTRODUCTION

Modern electron microscopy, due to the picometer wavelength of high-energy electron beam and the recent advances in aberration-correction and direct detector technologies, enables imaging of matter with atomic resolution (1–3). Together with the progress made in electron crystallography, tomography, cryo–single-particle imaging, and other analytical methods (4–9), it has become a central tool in many fields of research from materials science to biology (10–12). In a typical conventional electron microscope, the electron beam is produced by a thermionic or field emission process without any control over its temporal behavior. With such an electron source, images are either static or taken at long time intervals because of the limitation of the millisecond refresh rate of conventional electron detectors. To investigate the reaction paths in physical and chemical transitions beyond the detector limitations, the advanced electron microscope requires a high temporal resolution.

Controlled emission or modulation of a pulsed electron beam is a proven method to produce time-resolved electron microscopy for studying the elementary dynamical processes of structural and morphological changes, i.e., ultrafast electron microscopy (UEM) (13–15). Several methods have been developed to achieve a pulsed electron beam in an electron microscope, such as the electrostatic beam blanker (16–18) and laser-actuated photoemission (19–24), which make nanosecond and sub-picosecond (respectively) dynamics accessible. For the former, the intrinsic nanosecond duration of the electron pulse largely restricts the temporal resolution. For the latter, further optimization of the photoemitted electron pulse using microwave compression (25, 26), terahertz compression (27–31), active control via radio frequency (RF) optics (32, 33), or photon gating

(34, 35) can extend the temporal resolution into the deep femtosecond regime, which finds vast applications in studying the transient structures and morphologies of inorganic and organic materials (13, 19, 36). Therefore, the laser-actuated photoemission scheme is currently the primary method for UEM. However, several barriers exist for achieving laser-actuated photoemission: Femtosecond lasers can be bulky and expensive, instrumental modifications are intricate, and beam fluctuation is an intrinsic problem due to the inevitable laser pointing instabilities on the cathode. Moreover, the excitation for samples is generally limited to the same femtosecond laser source, which not only produces significant heating but also has been largely incompatible with the study of device physics, especially the high-frequency electrodynamics. Electrodynamics of devices, particularly in the gigahertz range, is fundamentally important because the standards of global data transfer (Wi-Fi, 4G, 5G, processor clock speeds, etc.) and RF microelectromechanical systems (MEMS) are almost all in the gigahertz range (37, 38).

It has been proposed that chopping a continuous electron beam through the combination of a resonant RF deflection cavity and a small aperture holds promise as an alternative to create short electron pulses for the implementation of a laser-free UEM (39–42), where the continuous beam is periodically swept across the aperture, resulting in a pulsed beam conserving the original peak brightness and energy spread. The advantage is that no femtosecond lasers and intrusive alterations to the electron source are required. However, the resonant RF deflection cavity can only operate at a particular resonance frequency that is sensitive to the ambient thermal fluctuation and requires a very high RF power for actuation. Furthermore, the resonant RF deflection cavity will induce a dual pulsed beam due to the inevitable creation of two pulses with different divergence angles in each RF period. So far, no ultrafast pump-probe imaging or diffraction by the proposed RF cavity–driven UEM has been achieved.

Here, we report the development of a laser-free UEM by integrating a prototype RF-driven electron beam pulser to create short electron pulses with a tunable repetition rate from 100 MHz up to 12 GHz, which provides the capability to record ultrafast images and diffraction patterns of structure transitions. With optimization of the input RF power and frequency for the pulser, we achieved a

[1]Condensed Matter Physics and Material Science Department, Brookhaven National Laboratory, Upton, NY 11973, USA. [2]School of Physics, Nankai University, Tianjin 300071, China. [3]Collider-Accelerator Department, Brookhaven National Laboratory, Upton, NY 11973, USA. [4]Euclid Techlabs LLC, 365 Remington Blvd., Bolingbrook, IL 60440, USA. [5]Microsystems and Nanotechnology Division, National Institute of Standards and Technology, Gaithersburg, MD 20899, USA. [6]Materials Science and Engineering Division, National Institute of Standards and Technology, Gaithersburg, MD 20899, USA.
*Corresponding author. Email: zhu@bnl.gov (Y.Z.); xwfu@nankai.edu.cn (X.F.)

~10-ps time resolution in our instrument. Moreover, the same broadband tunable RF signal can be used to provide sample excitation. As a first demonstration of its capability for studying ultrafast dynamics, we carried out a pump-probe study on electromagnetic (EM) wave propagation dynamics in a microstrip specimen consisting of two interdigitated combs, one of the basic building blocks for RF MEMS (43). Under a 5.25-GHz EM wave excitation, the stroboscopic imaging reveals, in real time and space, unambiguous temporal oscillating EM fields around the tines of the combs with time-dependent polarization direction and strength. Moreover, a clear local field enhancement appears at the corners of each tine. Combining numerical simulations and experimental results, we have uncovered the electrodynamics of a gigahertz EM wave propagation in the microstrip specimen, which is fundamentally essential to the operation of most information processing devices and currently inaccessible by other imaging methods.

RESULTS AND DISCUSSION

We present the conceptual design of the laser-free UEM schematically in Fig. 1A, which outlines the interfacing of the RF-driven pulser system with a transmission electron microscope (TEM). Figure 1B shows a picture of our prototype laser-free UEM system based on a 200-keV TEM (JEOL JEM-2100F, a Lorentz TEM with a Schottky field emission source) (44). The pulser, inserted between the electron gun and the microscope's first condenser lens, consists of two traveling wave metallic comb stripline elements with a small chopping aperture between them (inset of Fig. 1). The details of the design have been described elsewhere (42, 45, 46). Briefly, the top stripline element is an electron beam modulator (K1), while the bottom one is a demodulator (K2), and both operate in the traveling wave mode. The input RF signals to K1 and K2 have the same frequency and are phase-locked to a master oscillator, while their amplitude (i.e., power) and relative phase are digitally tunable. When the pulser is driven by an RF signal with the frequency of f_0, a sinusoidal EM field is generated in the modulator K1, introducing an oscillating transverse momentum kick (in the x-y plane, where z is the optic axis) to the incoming continuous electron beam. The beam begins to oscillate in the x-y plane and sweep across the chopping aperture. The chopping aperture partitions the continuous beam into periodic electron pulses with a repetition rate of $2f_0$, because two pulses are created in each RF cycle. Further downstream, as the pulses enter the demodulator K2, a phase and amplitude optimized oscillating EM field established in K2 fully compensates the transverse momentum induced by K1 to reduce the emittance growth and energy spread of the pulses, preserving the spatial and temporal coherence. Note that the K2 compensation
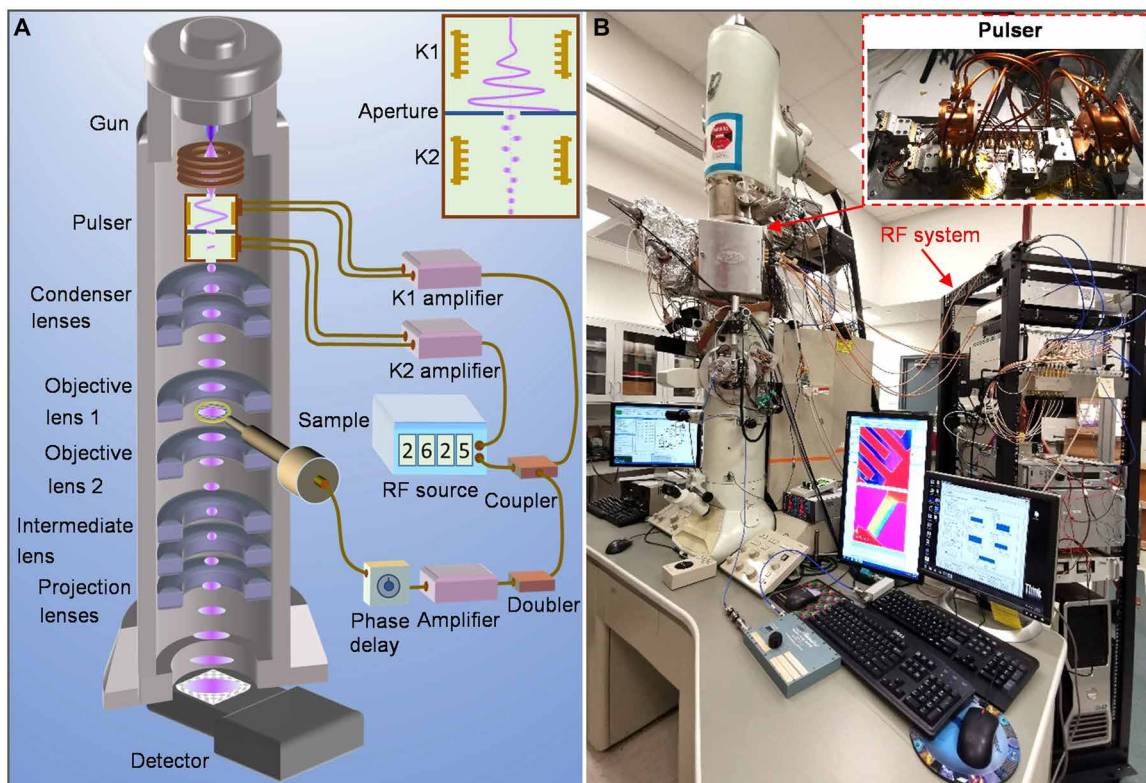

Fig. 1. Laser-free UEM system. (**A**) Schematic of the conceptual design of the laser-free UEM. The TEM with the integration of an RF-driven pulser system and a frequency-doubled, delay-controlled RF circuit for the sample excitation is shown. The pulser is inserted between the electron gun and the standard column lens. The inset shows a schematic design of the pulser, which consists of two traveling wave metallic comb stripline elements: the modulator K1 and the demodulator K2, with a chopping aperture between them. The modulator K1 sweeps the continuous electron beam across the chopping aperture to create two electron pulses in each RF cycle, while the demodulator K2 compensates the K1-induced transverse momentum on the pulses to further rectify the shape of the chopped beam. (**B**) Photograph of our homebuilt laser-free UEM system based on a JEOL JEM-2100F Lorentz TEM. The TEM with the RF-driven pulser inserted between the electron gun and the standard column lens and the connected RF source are shown. The inset shows a picture of the modulator K1, the demodulator K2, and the chopping aperture inside the pulser. Photo credit: Xuewen Fu, School of Physics at Nankai University.

plays a critical role for resolving the dual pulsed beam issue due to the modulator-induced transverse momentum on the chopped pulses (39, 40), which is crucial to realize the ultrafast pump-probe measurements. Because both K1 and K2 operate in the traveling wave mode, a broadband EM field with a frequency ranging from 50 MHz to 6 GHz can be established in our current design. Thus, because of the frequency doubling, the repetition rate of the electron pulse is tunable from 100 MHz to 12 GHz. Unless otherwise specified, the RF frequency of $f_0 = 2.625$ GHz is used for all the experimental data presented in this work.

To perform true ultrafast pump-probe experiments, the sample should be excited at the same repetition rate as the probe electron pulses. For the EM wave excitation configuration (Fig. 1), because the repetition rate of the pulsed beam is $2f_0$, we split a small part of the RF signal (~10% of the power) from the RF source of K1 by a coupler and doubled its frequency to $2f_0$ with a frequency doubler. After a downstream amplifier, a phase shifter is used to control the time delay (i.e., phase delay) between the excitation EM wave and the probe electron pulse. Last, we use a specially designed TEM sample holder with broad bandwidth and low power loss to efficiently deliver the EM wave to the sample (Fig. 1). Moreover, using advanced laser-RF synchronization technologies with little pulse jitter (31, 47), the excitation for samples is extensible to laser pulses, namely, the laser-triggered pump-probe experiments could be performed as well with our instrument and an appropriate laser-compatible sample holder.

The rationale behind the design of the RF-driven pulser is to realize laser-free UEM while preserving the original modalities of the TEM when the RF activation is off. To test the performance of the TEM after integrating the pulser, we recorded a set of imaging and diffraction results under the same condition in both continuous

beam (conventional TEM) mode and pulsed beam mode (Fig. 2). At the maximum magnification (200,000×) of this Lorentz TEM with a field-free weakly excited objective lens, the bright-field images of gold nanoparticles in both modes are comparable in both intensity profile and contrast (Fig. 2, A and E). For the out-of-focus Fresnel phase imaging, both modes show similar phase contrast for a magnetic vortex in a circular ferromagnetic permalloy disc (Fig. 2, D and H). For the diffraction tests, diffraction patterns of gold nanoparticles (Fig. 2, B and F) and a VO_2 single crystal (Fig. 2, C and G) were recorded in both modes, which exhibit no obvious change other than the expected intensity decline in the pulsed beam mode. The comparable quality of imaging and diffraction between the pulsed beam mode and the continuous beam mode illustrates the good performance and versatility of our prototype laser-free UEM.

The temporal resolution of the laser-free UEM is mainly determined by the duration of the chopped electron pulses, which depends on the duty cycle of the chopped electron beam and can be altered independently by changing the input RF power (P_{rf}), frequency, and/or the chopping aperture size. Theoretically, the chopped pulse duration is given by $\tau = \gamma m_e(d + r)/4qE_0l$ (39), where γ is the Lorentz factor, m_e is the electron mass, d is the diameter of the chopping aperture, r is the diameter of the electron beam at the position of the chopping aperture, q is the elementary charge, E_0 is the EM field in K1, and l is the distance between K1 and the chopping aperture. Experimentally, when the beam waist at the chopping aperture is smaller than the aperture diameter, the pulse duration τ can be retrieved by measuring the ratio r of the total electron counts per second of the chopped beam and the continuous beam with the full beam illuminating on the camera (40), i.e., $\tau = r/2f_0$. As presented in Fig. 3A, the measured electron pulse duration decreases with increasing voltage amplitude (U_0) of the input RF source for the modulator
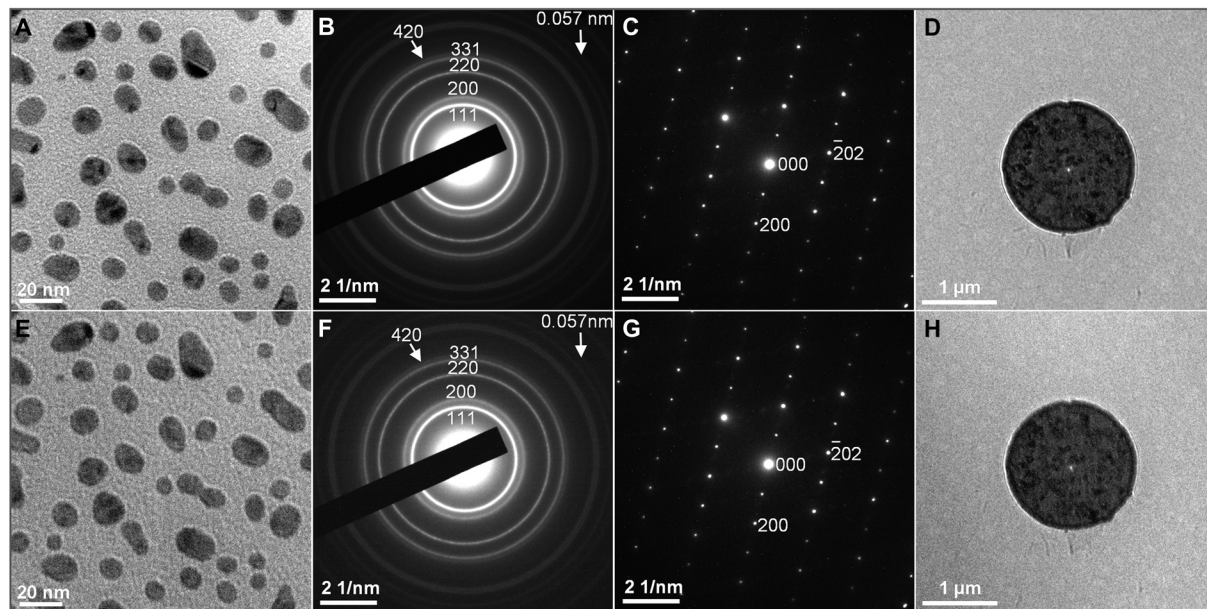

Fig. 2. Comparison of imaging and diffraction quality between the continuous beam mode and the pulsed beam mode. Images and diffraction patterns acquired at the continuous beam mode: (**A**) bright-field image of gold nanoparticles, (**B**) diffraction pattern of gold nanoparticles, (**C**) diffraction pattern of a VO_2 single crystal (along [010] zone axis), and (**D**) out-of-focus Fresnel phase image of magnetic vortex in a circular ferromagnetic permalloy disc. Images and diffraction patterns acquired at the pulsed beam mode with the repetition rate of 5.25 GHz: (**E**) bright-field image of gold nanoparticles, (**F**) diffraction pattern of gold nanoparticles, (**G**) diffraction pattern of a VO_2 single crystal (along [010] zone axis), and (**H**) out-of-focus Fresnel phase image of magnetic vortex in a circular ferromagnetic permalloy disc.
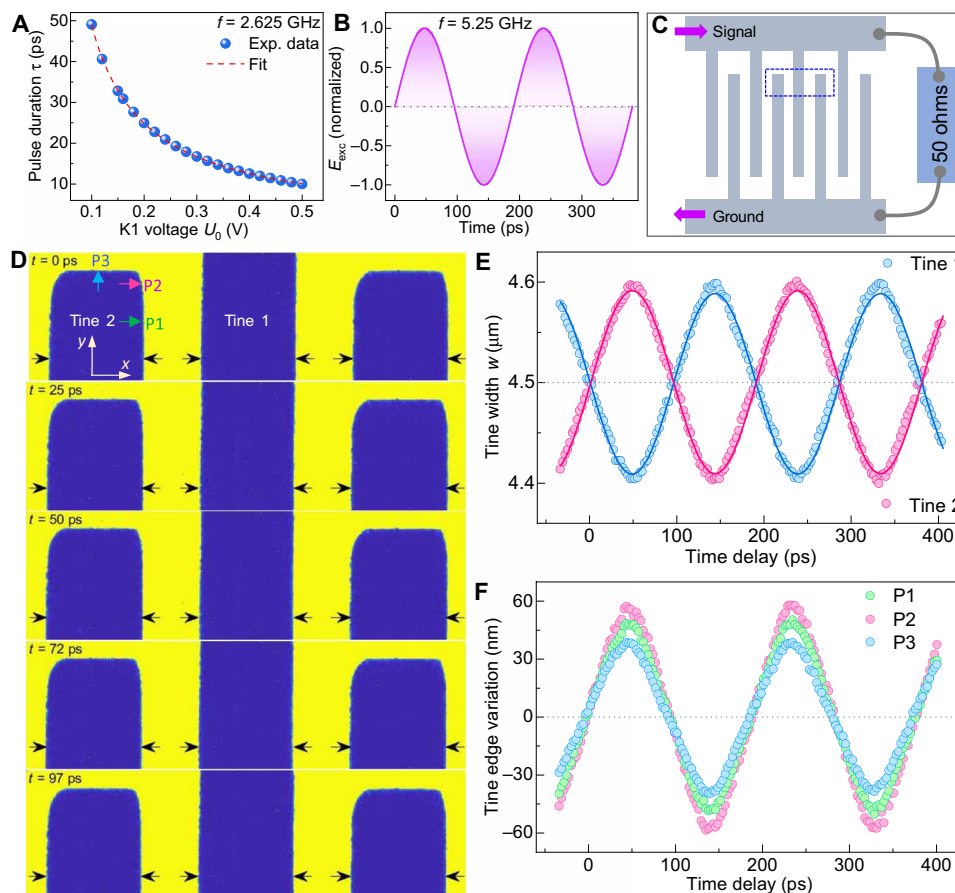
Fig. 3. Pump-probe imaging of the EM wave propagation dynamics in a microstrip of two interdigitated combs. (**A**) Electron pulse duration as a function of the voltage amplitude U_0 of the input RF source for the modulator K1. The red dashed line is the curve fit with an inverse function of $\tau \propto 1/U_0$. (**B**) Schematic of the temporal oscillating electric field (normalized in the field strength) of a 5.25-GHz EM wave used for excitation. (**C**) Schematic of two interdigitated combs used for investigation (fig. S1). The excitation signal is applied from one end of the two combs, while the other end is terminated with a 50-ohm load to eliminate the EM wave reflections. (**D**) Typical snapshots of two ground tines and one active tine in between them at different delay times (movie S1), obtained from the area indicated by the blue dashed box in (C). The images are acquired at a magnification of ×1200 with an integral time of 1.5 s. The arrows indicate the initial positions of the two edges of each tine in the images without excitation. (**E**) Width variations (along the x direction) of the active (blue dots) and ground tines (red dots) due to the beam deflection as a function of delay time with curve fitting. They follow a cosine function and a sinusoidal function, respectively, with the same amplitude and frequency. (**F**) Time-dependent imaging breathing of the tine's edge at three representative positions (P1, P2, and P3) around a ground tine, respectively, as indicated by the colored arrows in the first panel of (D). Position P2 near the tine's corner exhibits a much higher breathing amplitude than the other two positions, indicating a remarkable local field enhancement.

K1 and follows the theoretically expected behavior $\tau \propto 1/U_0 \propto 1/\sqrt{P_{rf}}$ (fit in Fig. 3A) (*39*). At the maximum input RF power of ~8 W and using the minimum chopping aperture of ~25 μm in our current design, the shortest pulse duration of ~10 ps is achieved. In principle, using higher input RF power, a higher RF frequency, and/or a smaller chopping aperture could achieve shorter and even subpicosecond or femtosecond electron pulses (*40*), which holds promise to further improve the temporal resolution.

To demonstrate the ultrafast pump-probe measurement capability of our laser-free UEM, we carried out an ultrafast imaging study on the EM wave propagation dynamics in a microstrip consisting of two interdigitated combs (Fig. 3C and fig. S1). Understanding electrodynamics in microstrips is important, as the oscillating currents and fields are fundamental to the operation of almost any information processing device (*28*). However, directly visualizing the electrodynamics at gigahertz frequencies in microstrips has not been achieved so far to the best of our knowledge because of the lack of

proper transient imaging technology. The sample was fabricated on a silicon-on-insulator (SOI) wafer and using a typical SOI microfabrication process (Materials and Methods) and was designed to match the wave impedance at around 5 GHz, which is the frequency regime for the advanced 5G wireless communication technologies. Specifically, the total length of each comb is 1.25 mm, and the tine pitch on both combs is 16 μm. The width and length of each tine are $w = 4.5$ μm and $L = 75$ μm, respectively, with a gap between the interleaved tines of $g = 3.5$ μm (fig. S1). The thickness of the tines along the beam-path direction is $D_z = 25$ μm. In the experiment, the input terminal of one comb was excited by a 5.25-GHz EM wave with a power of ~1.0 W (Fig. 3A), while the output end of the same comb was terminated with a 50-ohm load to eliminate signal reflections (Fig. 3C). The other comb was held at ground potential. The wavelength of the gigahertz wave for excitation is about 11.5 cm in vacuum but only about 3 cm in our microstrip because of the large relative permittivity (~12) of the silicon layer. Thus, the 1.25-mm comb sample

spans less than 5% of a full wave. Under the gigahertz wave excitation, the intentional local EM fields around the tines of the interdigitated combs would give a deflection to the imaging electron pulse in the x-y plane and result in a change in the image. Because the electron pulse duration is nearly 19 times shorter than the cycle (~190 ps) of the excitation EM wave, it allows us to take stroboscopic images at a series of specific delay times for time-frozen electrodynamics in the sample.

First time-resolved images of EM propagation in the interdigitated comb structure acquired at a magnification of 1200× with an integral time of 1.5 s are shown in Fig. 3D (movie S1), where a set of typical snapshots (two ground tines and one active tine in between them) at different delay times obtained from the area indicated by the blue dashed box in Fig. 3C is presented, revealing a pronounced temporal oscillation or breathing of the tines in the time-frozen images. With the delay time increasing from 0 ps (time zero was set at a delay point when the beam has no deflection), the width of the middle active tine gradually shrinks first and then broadens, while the width of the two ground tines gradually broadens first and then shrinks in alternation. More specifically, the retrieved width variation (along the x direction) versus time of the two ground tines follows a sinusoidal function (red dots in Fig. 3E, only showing the data for one of the ground tines), while that of the active tine follows a cosine function (blue dots in Fig. 3E). Through the fitting, it is found that the width variations of both the active and ground tines show a similar amplitude (~90 nm) and have an identical frequency of 5.25 ± 0.02 GHz (Fig. 3E), which is consistent with the frequency of the gigahertz wave for excitation.

For a more rigorous analysis of the experimental result, we denote the spatiotemporal electric and magnetic fields around the tines as $E(x, y, z, t)$ and $B(x, y, z, t)$, the electron pulse velocity as v_e, and the frequency of the excitation wave as f. Considering the following conditions: (i) $D_z/v_e \ll 1/f$, the electron penetration time through the sample is much shorter than the cycle of the excitation wave, where D_z is the thickness of the sample along the beam-path direction; (ii) the pulse duration is nearly 19 times shorter than the periodicity of the excitation wave; (iii) the effects of magnetic fields are negligible compared to those of the electric fields for the specimen geometry (28); and (iv) the pulsed beam is collimated at the sample. The approximate change in beam divergence angles $\alpha_{x, y}$ after penetrating the sample at each position in the beam and at a delay time of t is given by $\alpha_{x,y}(x, y, t) \approx q E_{x,y}(x, y, t) D_z/m_e v_e^2$ (28). At a specific

delay time t, if the electric field vectors (in the x-y plane) around a tine point outward from the tine's surface, then each ray in the pulsed beam is subjected to a field-dependent momentum kick toward the tine's surface and thus a change of divergence angle $\alpha_{x, y}(x, y, t)$, resulting in a beam deflection toward the tine's surface and a shrinking of the tine in the image; in contrast, if the electric field vectors point toward the tine's surface, then both the momentum kick and the beam deflection are outward from the tine's surface, resulting in a broadening of the tine in the image. Therefore, the observed inverse temporal breathing of the active and ground tines indicates that, upon the EM wave excitation, an oscillating electric field perpendicular to $\vec{v}_e$ is built in the gaps between the active and ground tines. These images are a direct reflection of the EM wave propagation process through the interdigitated combs.

Considering a collimated beam illumination, the temporal electric field $E_{x, y}(x, y, t)$ around the tine is proportional to the change of the tine's edge intensity profile in the time-frozen images (28), namely, a larger beam deflection corresponds to a larger local electric field. The time-dependent imaging breathing (tine's edge variation) at three representative positions (P1, P2, and P3) around a ground tine is shown in Fig. 3F, as indicated by the colored arrows in the top panel of Fig. 3D. All of them follow the same cosine function but with different amplitudes. Point 2 near the tine's corner exhibits a much bigger amplitude than the other two positions, implying that there is a substantial local field enhancement at the corners of the tines in the EM wave propagation process, which will be discussed later.

We further studied the dependence of EM wave propagation dynamics on the excitation power. Additional ultrafast pump-probe imaging measurements were performed with different excitation powers from 0.5 to 1.0 W, where a similar temporal breathing phenomenon of the active and ground tines occurred at all different powers. Figure 4A presents the plots of the time-dependent width variation of a ground tine at all excitations, in which all the plots follow a sinusoidal function with the frequency of 5.25 ± 0.02 GHz (fitting in Fig. 4A), with no phase difference. While their amplitude increases with increasing excitation power and follows a square root dependence of the power (fit in Fig. 4B), i.e., the amplitude of the temporal oscillating electric field erected between the tines, as theoretically expected, changes as a square root function of the excitation power within this power range.

To further understand the experimental observations, we performed numerical simulations on the EM wave propagation in a
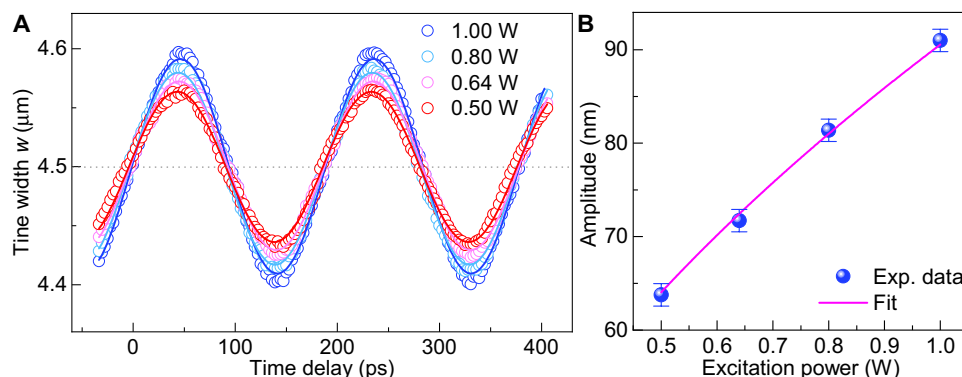

Fig. 4. Excitation power dependence of the EM wave propagation dynamics. (**A**) Plots of the time-dependent width variation of a ground tine at different delay times with increasing excitation power from 0.5 to 1.0 W. (**B**) The amplitude of the tine's width variation as a function of excitation power. It follows a square root dependence.

microstrip of two interdigitated combs with the same geometry and materials (fig. S2). The simulation was carried out by a three-dimensional (3D) EM finite element analysis package CST Microwave Studio (Materials and Methods). Hexahedron and locally refined meshes were adopted to get high-resolution EM field distribution along the sample. A frequency domain solver was used to solve Maxwell's equations in the cells. The 5.25-GHz RF signal (power of 1.0 W) excites a traveling EM wave, which propagates through the two interdigitated combs and is fully absorbed by the RF dump (load) at the end of the sample (fig. S2).

Figure 5A presents a set of typical snapshots of the simulated electric field distribution (projected in the x-y plane at the mid-comb thickness) around one active tine and two adjacent ground tines at different delay times (movie S2), where the arrows indicate the direction of the fields and the field strength is encoded in the color. The sample is nonmagnetic, and the effects of magnetic fields are negligible in the experiment, which are not considered here. Clearly, as the EM wave propagates through the interdigitated combs under investigation, a temporal oscillating electric field $E_{x,y}(x, y, t)$ is instantly established in between the gaps (in the x-y plane) of the active and ground tines, and the electric field is perpendicular to the tine's surface along the beam direction. Specifically, with time elapses from 0 to 95 ps, the fields point from the active tine toward the neighboring ground ones and gradually grow from zero to a maximum amplitude ($|E_x| \approx 1.7 \times 10^6$ V/m) at ~48 ps and then return back to zero at ~95 ps. Further, from 95 to 190 ps, the electric fields switch direction and gradually increase to a maximum amplitude ($|E_x| \approx 1.7 \times 10^6$ V/m) at ~143 ps and then decline to zero again at ~190 ps. This process is repeated with each EM wave cycle. These temporal oscil-

lating electric fields would exert a local field–dependent momentum kick on the imaging electrons that is proportional to the local waveform, resulting in the beam deflection and the breathing of the tines in the time-frozen images observed in the experiment. To show more clearly the temporal evolution of the field distribution, we plot the electric fields E_x and E_y as a function of time at three positions near a ground tine (P1, P2, and P3, in line with that in the experiment shown in Fig. 3D) in Fig. 5 (B and C, respectively). The electric fields at all three positions oscillate in a sinusoidal function with the frequency of 5.25 GHz but with different field amplitudes. In particular, the field strength (E_x) near the tine's corner is stronger than the other two positions. At the position of P1, E_y is nearly zero, while at the position of P3, E_x is almost zero. These results demonstrate that the electric field vectors are vertically polarized to the surface of the tines and undergo a synchronous oscillation in both direction and strength with time, while the corners of each tine exhibit a substantial local field enhancement. To see more clearly the local field enhancement, we plotted the electric field strength $|E_x|$ (in absolute value) at $t = 20$ ps as a function of position near the surface of a ground tine in Fig. 5D (2D map of the field strength is shown in fig. S3), where the positions are indicated by the red line with an arrow in the inset. As the position moves along the pink arrow, the field strength shows no apparent change in the parallel gap (from 0 to 20 μm), while it exhibits a sharp increase near the corner (position P2 indicated by the pink arrow) and then gradually decreases to zero, indicating the existence of a remarkable nonlinear local field distribution and an enhancement at the singular points of the microstrip in the EM wave propagation process. These nonlinear local field distribution and enhancement are caused by the convex
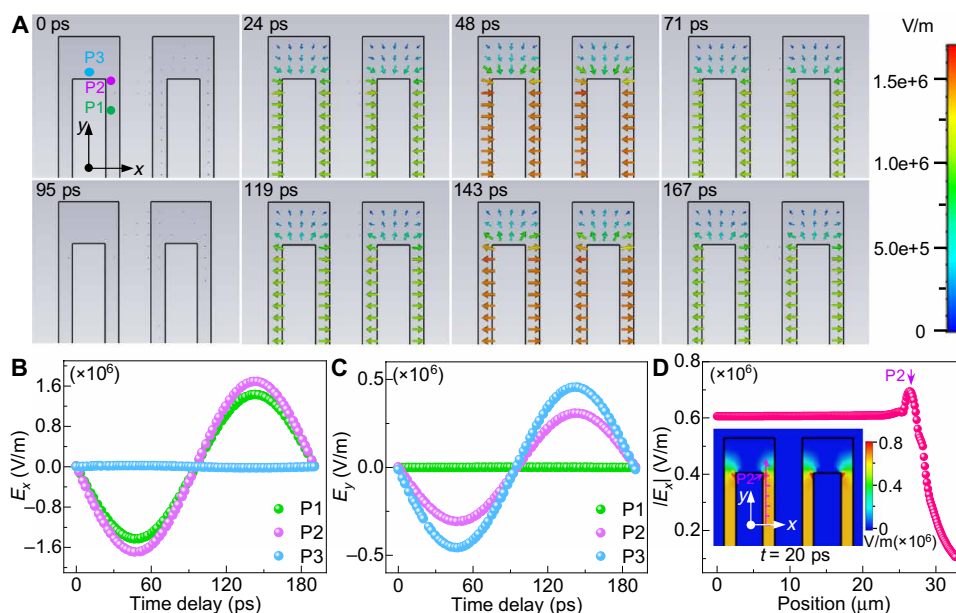

Fig. 5. Numerical simulations on the EM wave propagation dynamics in two interdigitated combs. (**A**) Typical snapshots of the simulated electric field distribution (projected in the x-y plane at the mid-comb thickness) around the active and ground tines at different delay times (movie S2). The arrows indicate the direction of the electric fields with encoded color for the field strength. (**B**) Plots of the electric field E_x as a function of time at three representative positions (P1, P2, and P3) around a ground tine. The field strength near the corner of the tine is stronger than other positions, indicating a local field enhancement near the corner. (**C**) Plots of the corresponding electric field E_y as a function of time at the three representative positions. The field strength of E_y at P1 is nearly zero and that of E_x at P3 is almost zero, which indicates that the established local field vectors are vertical to the tine's surfaces along the beam-pass direction. (**D**) Plot of the electric field strength of $|E_x|$ (in absolute value) as a function of position along the red line with an arrow (inset) near the surface of a ground tine. The sharp increase of the field strength near the corner (position P2) indicates a remarkable local field enhancement. The field strength in the inset is color-coded with the color bar in the inset.

surface geometry, where the smaller radius of the curved surface will result in a higher density of the equipotential surfaces and thus a larger local electric field. The results of the simulation are in good agreement with the experimental observations.

In summary, we developed a laser-free UEM with high spatiotemporal resolution by integrating an RF-driven pulser with a commercial TEM, which allows facile operation in both the UEM mode and the conventional TEM mode. It offers a universal methodology for EM wave excitation and structure dynamic studies in real time and space by using a straightforward retrofit. We used the laser-free UEM to study the gigahertz EM wave propagation dynamical process in a microstrip consisting of two interdigitated combs and demonstrated its ability for direct visualization of EM field oscillation with time, revealing field amplitude, polarization direction, and wave propagation on the nanometer-picosecond time scale, which has not been accessible by other imaging methods. The demonstrated laser-free UEM provides a powerful methodology for real-space visualization of electrodynamics in small devices operating from megahertz to gigahertz frequencies, such as the collective carrier dynamics and field effects in miniaturized wireless antennas, sensors, and RF MEMS (48). Future optimization of the input RF waveform and using a smaller chopping aperture could achieve sub-picosecond and even ~100-fs electron wave packets (39, 40), making femtosecond time resolution for the laser-free UEM possible. The laser-free UEM is also compatible with laser, current, and magnetic field–triggered ultrafast pump-probe measurements using advanced laser-RF and electricity-RF synchronization technologies (47). With these advanced features of the laser-free UEM, we envision the emergence of broad applications in many research areas, from materials physics to biology and mobile communication technologies.

MATERIALS AND METHODS
Sample preparation
Fabrication of the microstrip sample of interdigitated combs begins with an SOI wafer, using bulk semiconductor processing techniques common in MEMS fabrication. The starting SOI wafer has a 25-μm-thick device layer of <100> silicon with a resistivity of 0.01 ohm·cm, a 2 ± 0.5–μm–thick buried oxide layer, and a 500-μm-thick handle wafer. Metallic bond pads consisting of 10-nm/300-nm Cr/Au layers are deposited and patterned on the device layer using electron beam evaporation and a liftoff process. After metallization, 600-nm-thick SiO_2 hard mask layers are deposited on both sides of the wafer using plasma-enhanced chemical vapor deposition and patterned using optical lithography and reactive ion etching (RIE). The optical lithography patterns on the top surface (device layer) define the contours of the interdigitated comb. The comb patterns are etched into the Si device layer using deep RIE (DRIE), with an optimized process that yields smooth sidewalls and stops at the buried oxide layer. The wafer is flipped, and large rectangular etch windows are patterned on the back surface and aligned to the combs on the top surface. A second faster DRIE process is used on the back surface to etch through the entire thickness of the handle wafer, stopping at the bottom of the buried oxide layer. Individual dies are separated in this process. The combs are mechanically released from the substrate by etching away the SiO_2 hard mask and buried oxide using vapor-phase hydrofluoric acid etching. The resulting comb structure is thus structurally composed of only monolithic low-resistivity <100> silicon. The sample is mounted on a customized TEM chip carrier, and signal pads are wire-bonded using an Al wedge bonding process.

Numerical simulation
The numerical simulation on the gigahertz EM wave propagation dynamical process in the interdigitated combs was carried out by a 3D EM finite element analysis package CST microwave studio. The frequency domain solver in the package was used to solve the Maxwell's equations along the entire space by the finite element method. First, the (ns, μm, GHz) units were chosen to match the size of the sample and RF source frequency. The 3D model and material properties followed the description of the silicon-metallic comb stripline specimen used in the experiment. Because of the resistivity and permittivity of silicon, the material power loss was considered as well. The background was modeled as vacuum with a magnetic boundary condition in the electron beam propagation direction, and an electric boundary condition perpendicular to the beam direction. The excited RF frequency was 5.25 GHz with bandwidth of 0.02 GHz. Adaptive refinement of tetrahedral mesh was used with a manually defined, locally refined mesh at the corner of the comb, where the mesh cell length is about 0.28 μm. The total mesh number for the entire geometry is about 4.2 million. The simulation includes two waveguide ports: one for input RF power and another one for a perfect absorber, such that no reflection was considered in this simulation. All the electric fields, magnetic fields, phase information, and current densities in 3D space were monitored and stored. The simulation ran until the accuracy of the final results was better than 1×10^{-5}.

The postprocessing included 3D field visualization; 3D field–to–2D plane projection and field-along-a-line evaluations were performed to obtain fig. S2 and Fig. 5.

SUPPLEMENTARY MATERIALS
Supplementary material for this article is available at http://advances.sciencemag.org/cgi/content/full/6/40/eabc3456/DC1

REFERENCES AND NOTES
1. P. E. Batson, N. Dellby, O. L. Krivanek, Sub-ångstrom resolution using aberration corrected electron optics. *Nature* **418**, 617–620 (2002).
2. R. Erni, M. D. Rossell, C. Kisielowski, U. Dahmen, Atomic-resolution imaging with a sub-50-pm electron probe. *Phys. Rev. Lett.* **102**, 096101 (2009).
3. Y. Jiang, Z. Chen, Y. Han, P. Deb, H. Gao, S. Xie, P. Purohit, M. W. Tate, J. Park, S. M. Gruner, V. Elser, D. A. Muller, Electron ptychography of 2D materials to deep sub-ångström resolution. *Nature* **559**, 343–349 (2018).
4. D. De Rosier, A. Klug, Reconstruction of three dimensional structures from electron micrographs. *Nature* **217**, 130–134 (1968).
5. A. Komeili, Z. Li, D. K. Newman, G. J. Jensen, Magnetosomes are cell membrane invaginations organized by the actin-like protein MamK. *Science* **311**, 242–245 (2006).
6. X. Li, P. Mooney, S. Zheng, C. R. Booth, M. B. Braunfeld, S. Gubbens, D. A. Agard, Y. Cheng, Electron counting and beam-induced motion correction enable near-atomic-resolution single-particle cryo-EM. *Nat. Methods* **10**, 584–590 (2013).
7. K. Kimoto, T. Asaka, T. Nagai, M. Saito, Y. Matsui, K. Ishizuka, Element-selective imaging of atomic columns in a crystal using STEM and EELS. *Nature* **450**, 702–704 (2007).
8. Z. Saghi, P. A. Midgley, Electron tomography in the (S)TEM: From nanoscale morphological analysis to 3D atomic imaging. *Annu. Rev. Mater. Res.* **42**, 59–79 (2012).
9. J. Zhou, Y. Yang, Y. Yang, D. S. Kim, A. Yuan, X. Tian, C. Ophus, F. Sun, A. K. Schmid, M. Nathanson, H. Heinz, Q. An, H. Zeng, P. Ercius, J. Miao, Observing crystal nucleation in four dimensions using atomic electron tomography. *Nature* **570**, 500–503 (2019).
10. P. W. Hawkes, J. C. Spence, *Science of Microscopy* (Springer Science & Business Media, 2008).
11. A. H. Zewail, *Physical Biology: From Atoms to Medicine* (Imperial College Press, 2008).
12. S. J. Pennycook, P. D. Nellist, *Scanning Transmission Electron Microscopy: Imaging and Analysis* (Springer Science & Business Media, 2011).
13. A. H. Zewail, J. M. Thomas, *4D Electron Microscopy: Imaging in Space and Time* (World Scientific, 2010).

14. B. Reed, M. R. Armstrong, N. D. Browning, G. H. Campbell, J. E. Evans, T. La Grange, D. J. Masiel, The evolution of ultrafast electron microscope instrumentation. *Microsc. Microanal.* **15**, 272–281 (2009).

15. L. Zhang, J. P. Hoogenboom, B. Cook, P. Kruit, Photoemission sources and beam blankers for ultrafast electron microscopy. *Struct. Dyn.* **6**, 051501 (2019).

16. G. S. Plows, W. C. Nixon, Stroboscopic scanning electron microscopy. *J. Phys. E Sci. Instrum.* **1**, 595–600 (1968).

17. O. Bostanjoglo, R. Elschner, Z. Mao, T. Nink, M. Weingärtner, Nanosecond electron microscopes. *Ultramicroscopy* **81**, 141–147 (2000).

18. I. G. C. Weppelman, R. J. Moerland, J. P. Hoogenboom, P. Kruit, Concept and design of a beam blanker with integrated photoconductive switch for ultrafast electron microscopy. *Ultramicroscopy* **184**, 8–17 (2018).

19. A. H. Zewail, Four-dimensional electron microscopy. *Science* **328**, 187–193 (2010).

20. B. Barwick, H. S. Park, O.-H. Kwon, J. S. Baskin, A. H. Zewail, 4D imaging of transient structures and morphologies in ultrafast electron microscopy. *Science* **322**, 1227–1231 (2008).

21. A. Yurtsever, A. H. Zewail, 4D nanoscale diffraction observed by convergent-beam ultrafast electron microscopy. *Science* **326**, 708–712 (2009).

22. F. Carbone, O.-H. Kwon, A. H. Zewail, Dynamics of chemical bonding mapped by energy-resolved 4D electron microscopy. *Science* **325**, 181–184 (2009).

23. A. Yurtsever, R. M. van der Veen, A. H. Zewail, Subparticle ultrafast spectrum imaging in 4D electron microscopy. *Science* **335**, 59–64 (2012).

24. X. Fu, B. Chen, J. Tang, M. T. Hassan, A. H. Zewail, Imaging rotational dynamics of nanoparticles in liquid by 4D electron microscopy. *Science* **355**, 494–498 (2017).

25. T. Van Oudheusden, P. L. E. M. Pasmans, S. B. van der Geer, M. J. de Loos, M. J. van der Wiel, O. J. Luiten, Compression of subrelativistic space-charge-dominated electron bunches for single-shot femtosecond electron diffraction. *Phys. Rev. Lett.* **105**, 264801 (2010).

26. M. R. Otto, L. René de Cotret, M. J. Stern, B. J. Siwick, Solving the jitter problem in microwave compressed ultrafast electron diffraction instruments: Robust sub-50 fs cavity-laser phase stabilization. *Phys. Rev. Lett.* **4**, 051101 (2017).

27. C. Kealhofer, W. Schneider, D. Ehberger, A. Ryabov, F. Krausz, P. Baum, All-optical control and metrology of electron pulses. *Science* **352**, 429–433 (2016).

28. A. Ryabov, P. Baum, Electron microscopy of electromagnetic waveforms. *Science* **353**, 374–377 (2016).

29. R. Li, M. C. Hoffmann, E. A. Nanni, S. H. Glenzer, M. E. Kozina, A. M. Lindenberg, B. K. Ofori-Okai, A. H. Reid, X. Shen, S. P. Weathersby, J. Yang, M. Zajac, X. J. Wang, Terahertz-based subfemtosecond metrology of relativistic electron beams. *Phys. Rev. Accel. Beams* **22**, 012803 (2019).

30. L. Zhao, Z. Wang, C. Lu, R. Wang, C. Hu, P. Wang, J. Qi, T. Jiang, S. Liu, Z. Ma, F. Qi, P. Zhu, Y. Cheng, Z. Shi, Y. Shi, W. Song, X. Zhu, J. Shi, Y. Wang, L. Yan, L. Zhu, D. Xiang, J. Zhang, Terahertz streaking of few-femtosecond relativistic electron beams. *Phys. Rev. X* **8**, 021061 (2018).

31. E. C. Snively, M. A. K. Othman, M. Kozina, B. K. Ofori-Okai, S. P. Weathersby, S. Park, X. Shen, X. J. Wang, M. C. Hoffmann, R. K. Li, E. A. Nanni, Femtosecond compression dynamics and timing jitter suppression in a THz-driven electron bunch compressor. *Phys. Rev. Lett.* **124**, 054801 (2020).

32. J. Williams, F. Zhou, T. Sun, Z. Tao, K. Chang, K. Makino, M. Berz, P. M. Duxbury, C. Y. Ruan, Active control of bright electron beams with RF optics for femtosecond microscopy. *Struct. Dyn.* **4**, 044035 (2017).

33. J. Rosenzweig, A. Cahill, V. Dolgashev, C. Emma, A. Fukasawa, R. Li, C. Limborg, J. Maxson, P. Musumeci, A. Nause, R. Pakter, R. Pompili, R. Roussel, B. Spataro, S. Tantawi, Next generation high brightness electron beams from ultrahigh field cryogenic rf photocathode sources. *Phys. Rev. Accel. Beams* **22**, 023403 (2019).

34. M. T. Hassan, J. Baskin, B. Liao, A. Zewail, High-temporal-resolution electron microscopy for imaging ultrafast electron dynamics. *Nat. Photonics* **11**, 425–430 (2017).

35. M. T. Hassan, H. Liu, J. S. Baskin, A. H. Zewail, Photon gating in four-dimensional ultrafast electron microscopy. *Proc. Natl. Acad. Sci. U.S.A.* **112**, 12944–12949 (2015).

36. W. E. King, G. H. Campbell, A. Frank, B. Reed, J. F. Schmerge, B. J. Siwick, B. C. Stuart, P. M. Weber, Ultrafast electron microscopy in materials science, biology, and chemistry. *J. Appl. Phys.* **97**, 111101 (2005).

37. A. A. Khan, M. H. Jamaluddin, S. Aqeel, J. Nasir, O. Owais, Dual-band MIMO dielectric resonator antenna for WiMAX/WLAN applications. *IET Microw. Antenna Propag.* **11**, 113–120 (2017).

38. Y. Zhang, L. Gao, X. Y. Zhang, Compact quad-band bandpass filter for DCS/WLAN/WiMAX/5G Wi-Fi application. *IEEE Microw. Wirel. Compon. Lett.* **25**, 645–647 (2015).

39. J. Van Rens, W. Verhoeven, E. Kieft, P. Mutsaers, O. Luiten, Dual mode microwave deflection cavities for ultrafast electron microscopy. *Appl. Phys. Lett.* **113**, 163104 (2018).

40. W. Verhoeven, J. Van Rens, E. Kieft, P. Mutsaers, O. Luiten, High quality ultrafast transmission electron microscopy using resonant microwave cavities. *Ultramicroscopy* **188**, 85–89 (2018).

41. A. Lassise, P. Mutsaers, O. Luiten, Compact, low power radio frequency cavity for femtosecond electron microscopy. *Rev. Sci. Instrum.* **83**, 043705 (2012).

42. J. Qiu, G. Ha, C. Jing, S. V. Baryshev, B. W. Reed, J. W. Lau, Y. Zhu, GHz laser-free time-resolved transmission electron microscopy: A stroboscopic high-duty-cycle method. *Ultramicroscopy* **161**, 130–136 (2016).

43. C. G. Christodoulou, in *Proceedings of the 2003 SBMO/IEEE MTT-S International Microwave and Optoelectronics Conference-IMOC 2003* (IEEE, 2003), vol. 1, pp. 525–531.

44. Certain commercial equipment, instruments, or materials are identified in this presentation to specify the experimental procedure adequately. Such identification is not intended to imply recommendation or endorsement by the National Institute of Standards and Technology, nor is it intended to imply that the materials or equipment identified are necessarily the best available for the purpose.

45. C. Jing, Y. Zhu, A. Liu, K. Schliep, X. Fu, Y. Zhao, E. Montgomery, W. Rush, A. Kanareykin, M. Katz, J. Lau, Tunable electron beam pulser for picoseconds stroboscopic microscopy in transmission electron microscopes. *Ultramicroscopy* **207**, 112829 (2019).

46. J. W. Lau, K. B. Schliep, M. B. Katz, V. J. Gokhale, J. J. Gorman, C. Jing, A. Liu, Y. Zhao, E. Montgomery, H. Choe, W. Rush, A. Kanareykin, X. Fu, Y. Zhu, Laser-free GHz stroboscopic transmission electron microscope: Components, system integration, and practical considerations for pump–probe measurements. *Rev. Sci. Instrum.* **91**, 021301 (2020).

47. F. Kiewiet, A. Kemper, O. Luiten, G. Brussaard, M. Van der Wiel, Femtosecond synchronization of a RF oscillator to a mode-locked Ti:sapphire laser. *Nucl. Instrum. Methods Phys. Res.* **484**, 619–624 (2002).

48. T. Nan, H. Lin, Y. Gao, A. Matyushov, G. Yu, H. Chen, N. Sun, S. Wei, Z. Wang, M. Li, X. Wang, A. Belkessam, R. Guo, B. Chen, J. Zhou, Z. Qian, Y. Hui, M. Rinaldi, M. E. McConney, B. M. Howe, Z. Hu, J. G. Jones, G. J. Brown, N. X. Sun, Acoustically actuated ultra-compact NEMS msssagnetoelectric antennas. *Nat. Commun.* **8**, 296 (2017).